Local field potentials of subthalamic nucleus contain electrophysiological footprints of motor subtypes of Parkinson's disease

Ilknur Telkes[a], Ashwin Viswanathan[b], Joohi Jimenez-Shahed[c], Aviva Abosch[d], Musa Ozturk[a], Akshay Gupte[e], Joseph Jankovic[c], and Nuri F. Ince[a,1]

[a]Department of Biomedical Engineering, University of Houston, Houston, TX 77204-5060; [b]Department of Neurosurgery, Baylor College of Medicine, Houston, TX 77030; [c]Parkinson's Disease Center and Movement Disorders Clinic, Department of Neurology, Baylor College of Medicine, Houston, TX 77030; [d]Department of Neurosurgery, University of Colorado School of Medicine, Aurora, CO 80045; and [e]Department of Neurosurgery, University of Minnesota Medical School, Minneapolis, MN 55455

Although motor subtypes of Parkinson's disease (PD), such as tremor dominant (TD) and postural instability and gait difficulty (PIGD), have been defined based on symptoms since the mid-1990s, no underlying neural correlates of these clinical subtypes have yet been identified. Very limited data exist regarding the electrophysiological abnormalities within the subthalamic nucleus (STN) that likely accompany the symptom severity or the phenotype of PD. Here, we show that activity in subbands of local field potentials (LFPs) recorded with multiple microelectrodes from subterritories of STN provide distinguishing neurophysiological information about the motor subtypes of PD. We studied 24 patients with PD and found distinct patterns between TD (n = 13) and PIGD (n = 11) groups in high-frequency oscillations (HFOs) and their nonlinear interactions with beta band in the superior and inferior regions of the STN. Particularly, in the superior region of STN, the power of the slow HFO (sHFO) (200–260 Hz) and the coupling of its amplitude with beta-band phase were significantly stronger in the TD group. The inferior region of STN exhibited fast HFOs (fHFOs) (260–450 Hz), which have a significantly higher center frequency in the PIGD group. The cross-frequency coupling between fHFOs and beta band in the inferior region of STN was significantly stronger in the PIGD group. Our results indicate that the spatiospectral dynamics of STN-LFPs can be used as an objective method to distinguish these two motor subtypes of PD. These observations might lead to the development of sensing and stimulation strategies targeting the subterritories of STN for the personalization of deep-brain stimulation (DBS).

Parkinson's disease | tremor dominant | postural instability and gait difficulty | local field potentials | microelectrode recordings

Parkinson's disease (PD) is a complex progressive neurodegenerative disorder with a broad spectrum of motor and nonmotor features (1). Despite the various subgroups determined by data-driven approaches (2–4), the tremor dominant (TD) and postural instability and gait difficulty (PIGD) groups are the earliest classification (5) of PD motor subtypes based on clinical evaluation (5, 6). Their categorization is based on clinical observations most often evaluated using the Unified Parkinson's Disease Rating Scale (UPDRS) or the revised version, the Movement Disorder Society (MDS)-UPDRS (5, 7). These outcome rating scales have been validated and are widely used for motor subtyping of PD patients (7–11). Studies have shown that TD patients have a relatively slow disease progression compared with PIGD patients who display a larger annual increase in symptom severity (12). Severe cognitive dysfunction is consistently seen in PIGD patients or PD patients with late onset, while TD patients or those with young onset show either a lesser degree or no cognitive impairment (13, 14). One study showed that signs of dementia appeared in TD patients only after PIGD symptoms developed (8). Despite the variation and overlap in

clinical features and in progression of the disease, the TD phenotype generally has better prognosis than the PIGD phenotype (1, 15). It has been proposed that different morphology, neurochemistry, and/or basal ganglia circuitry underlie the two PD subtypes (15–18). However, to our knowledge, no electrophysiological pattern linked to the two subtypes has been identified in the basal ganglia.

Deep-brain stimulation (DBS) of the STN is an effective therapy for the treatment of motor symptoms of PD (1). The ultimate goal of DBS surgery is placement of the DBS electrode within the motor territory of the STN, in a location that leads to the greatest therapeutic effect with the fewest side effects. Optimization of DBS for TD and PIGD subtypes (11) is one of the objectives of neuromodulation research. Although TD and PIGD motor subtypes of PD have been defined based on symptoms since the mid-1990s, no underlying neural correlates have yet been identified. The absence of a reliable neural marker of PD motor subtypes might lead to suboptimal treatment using DBS. Here, we tested the hypothesis that the spatiospectral patterns of local field potentials (LFPs) recorded with microelectrodes

Significance

Despite the fact that deep-brain stimulation (DBS) of the subthalamic nucleus (STN) has emerged as an effective surgical treatment for Parkinson's disease (PD), there is no available neurobiomarker providing information about the symptoms of PD subtypes in STN. In this paper, we report the finding of neural correlates of two motor phenotypes of PD in the territories of STN. Despite advances in imaging, microelectrode recording continues to be best practice and the dominant method for STN localization during DBS surgery [Abosch A, et al. (2013) Stereotact Funct Neurosurg 91:1–11]. Hence, we anticipate our findings will provide possibilities for the intraoperative interpretation of oscillatory dynamics of STN and that these well-localized patterns can be used as objective tools for future neuromodulation technologies.

NEUROSCIENCE

www.manaraa.com

from STN subterritories can be used to distinguish PD patients with PIGD or TD motor subtypes.

Results

We recorded LFPs from the stainless-steel ring electrode situated 3 mm above the microelectrode tip with a 1-mm width and a 0.7-mm diameter (*Materials and Methods*) (see Fig. 5*B*). In particular, we used microelectrode tracks targeting the STN in the hemisphere contralateral to the dominant motor symptoms and investigated the depth-varying spectral dynamics of the oscillatory neural activity by constructing depth–frequency maps (DFMs). In the TD group, we observed that the center frequency of HFOs shifted from low- to high-frequency range around 2 mm below the superior border of the STN. Therefore, with STN border representing 0 mm, we explored the differences between two PD groups in superior (from 0 to −2 mm) and inferior regions (from −2 to −5 mm) of the STN (*Materials and Methods*) (see Fig. 5*C*). We used the neural activity recorded from a 5-mm-long segment situated above the superior border of STN (from 0 to +5 mm) as a reference and investigated the relative power change of beta and HFOs within superior and inferior regions with respect to this reference. We also quantified the nonlinear interaction between beta and HFOs in terms of phase–amplitude coupling (PAC) in these subregions.

Spatiospectral Patterns of STN-LFPs. A total of 72 electrode tracks from 24 PD patients was studied. LFPs were recorded simultaneously from three microelectrodes per patient with a duration of an average of 20.7 s at each depth. Based on UPDRS or MDS-UPDRS scores of these patients, 13 of them were identified as TD and 11 as PIGD. These two subgroups showed no significant statistical difference in age, disease duration, or age onset ($t = -1.882$, $P = 0.073$; $t = -0.715$, $P = 0.482$; $t = -1.443$, $P = 0.163$, Student's t test). The scatterplot and the distribution of the tremor and gait-related scores of the patients are provided in Fig. 1. Although the ratio of mean tremor scores to mean gait-related scores shows well separation between groups as seen from the scatterplot (below and above the diagonal line, respectively) in Fig. 1*A*, the distribution of these scores in Fig. 1*B* shows that some of the TD and PIGD subjects have overlapping tremor and gait scores.

As shown in Fig. 1*C*, visual inspection of the raw LFPs indicated an increased oscillatory activity in both PIGD and TD patient populations upon the electrode entry into the STN. The difference of raw LFP power between recordings above the superior STN border (out-STN) and below the STN border (in-STN) was found to be statistically significant (in-STN vs. out-STN, $P < 0.001$, Wilcoxon's test) in both groups but without any distinction in between ($Z = 0.024$, $P = 0.981$, Mann–Whitney U test; Fig. 1*D*).

The DFMs, as shown in Fig. 2*A*, revealed distinct spatiospectral patterns of LFPs between TD and PIGD groups. In the TD group, a strong and quite localized 200- to 260-Hz activity was observed beginning at the superior STN border (0 mm) and extending 2 mm below it. These slow high-frequency oscillations (sHFOs) were well aligned both with beta oscillations (8–35 Hz) and with the superior border of STN and shifted to higher frequency deeper in the nucleus. No clear sHFO peak could be observed at the superior border in the average DFM of PIGD subjects (Fig. 2*A*, *Right*). The beta oscillations and HFOs in the PIGD group appeared slightly deeper following the entry into the STN. Spatiospectral patterns of LFP oscillations in STN were investigated in detail by dividing STN into (*i*) superior and (*ii*) inferior regions (Fig. 2*A*, panels with zoomed-in view) based on the location where a frequency shift in HFO occurs in the TD subtype. Once the electrodes advanced deeper, away from the border, it was noted that both groups demonstrated fast high-frequency oscillations (fHFOs) with wider bandwidth ranging from 260 to 400 Hz and with a significant difference between the
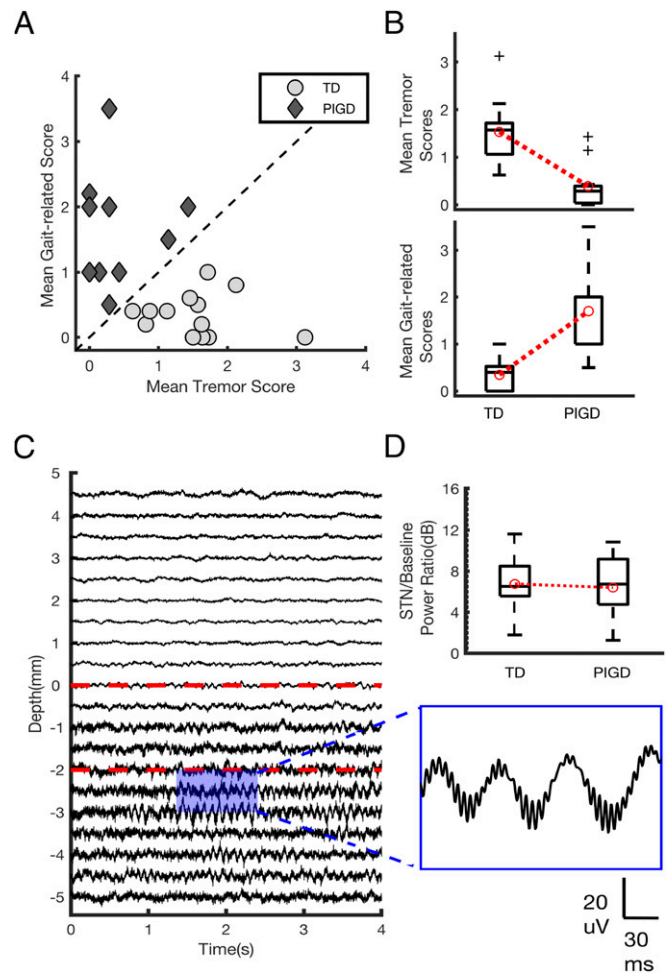
Fig. 1. Distribution of preoperatively obtained UPDRS scores and raw LFP data after projection. (*A*) Scatterplot shows the distribution of mean tremor and mean gait-related scores of all subjects. The circles represent TD (mean score, ≥1.5), and the diamonds represent PIGD (mean score, ≤1) subjects. The diagonal line separates the two phenotypes. (*B*) Boxplots showing the mean tremor and mean gait-related scores of patients in each phenotype. (*C*) LFPs recorded from multiple tracks are projected with GED method and a single virtual channel is obtained. The raw LFP data in each depth after projection are shown for a representative subject. Energy of LFPs in all subjects increases when the electrodes enter the STN. The superior border of STN and the separation line between superior and inferior region are marked as red dashed lines, respectively. Selected raw LFP signal segment indicates a visible PAC. (*D*) Boxplot shows the power ratio of STN to baseline in TD and PIGD groups. Both distributions are significantly greater than zero, indicating that LFP energy in STN is higher than the baseline energy.

peak frequencies (mean ± SD of TD, 290 ± 26 Hz; PIGD, 322 ± 32 Hz) of two groups ($Z = -2.479$, $P = 0.013$, Mann–Whitney U test). The averaged LFP spectra in superior and inferior subregions for each group are shown in Fig. 2*B*. The sHFO power in the superior subregion of the STN was significantly higher in the TD group compared with the PIGD group ($Z = 2.402$, $P = 0.016$, Mann–Whitney U test). However, no significant difference in sHFO power was found in the inferior subregion. Similarly, there was no significant difference noted in beta or fHFO power in these subregions between groups (Fig. 2*C* and *SI Appendix*, Note S1).

Cross-Frequency Interactions of LFPs in Subterritories of the STN. Fig. 3*A* shows the comodulograms estimated from individual depths in superior and inferior subregions of STN for a representative TD and a PIGD subject. The PAC analysis executed in

www.manaraa.com
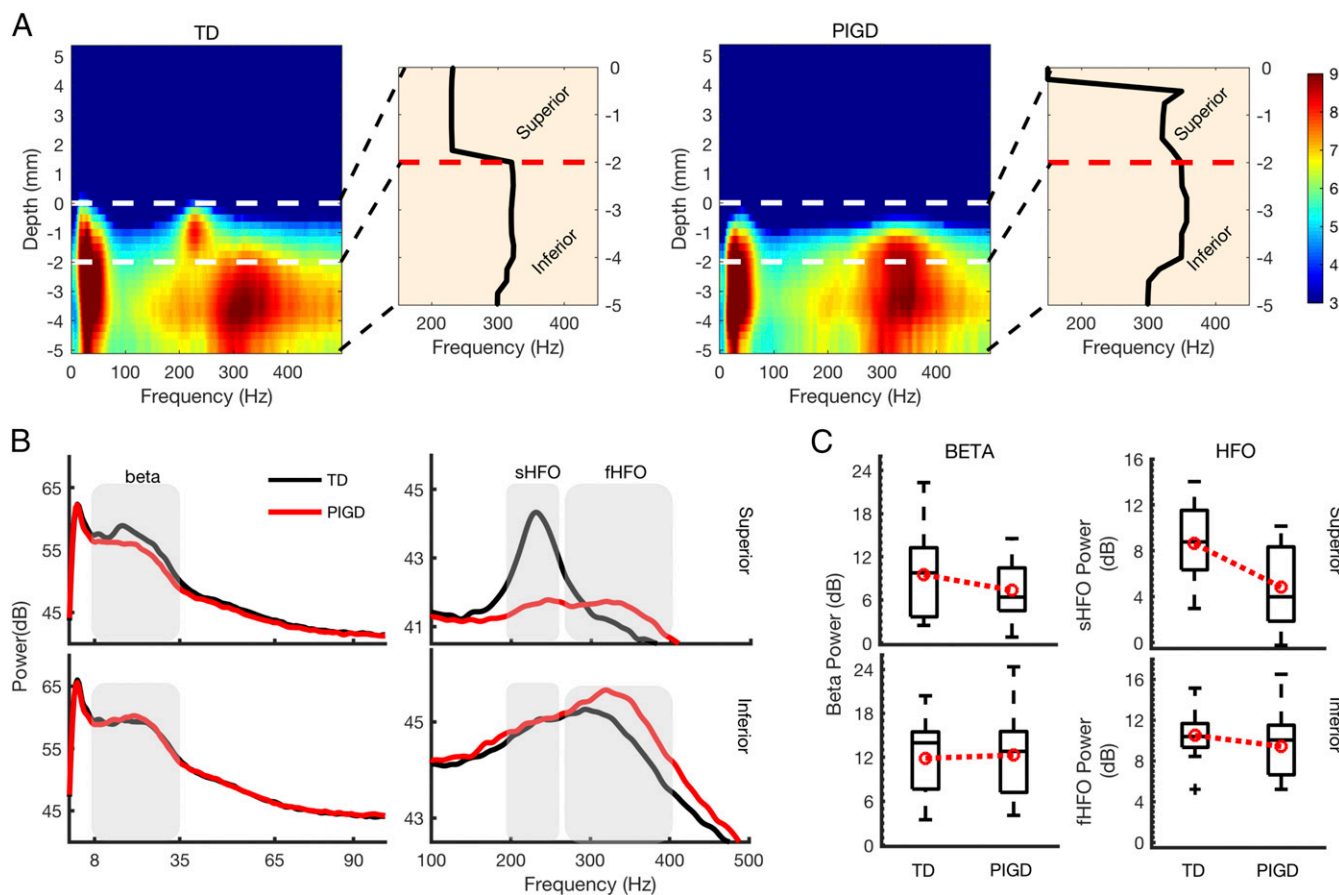
Fig. 2. Spatiospectral dynamics of LFPs in TD and PIGD groups. (*A*) Average DFMs of TD and PIGD groups aligned to 0 mm. The *x* axis represents the frequency, and the *y* axis represents the depths from superior to inferior direction. The white dashed lines at 0 mm show the single superior border obtained for each group. The color bar indicates the energy of the signal in decibel scale. The panels next to DFMs indicating the zoomed-in view of the spatial distribution of peak frequency between 150 and 450 Hz calculated from average DFMs in TD and PIGD groups. *Left* panel shows the 2-mm span of the shift from sHFO to fHFO in TD group (mean ± SD of depths of shift, 1.93 ± 1.46 mm). Since there is no clear shift in PIGD group, DFMs in all subjects were divided into superior and inferior regions based on the observations in TD group. (*B*) Average power spectra generated from superior and inferior regions showing the intergroup comparisons (black, TD; red, PIGD). *Top* row represents the superior average power spectra and *Bottom* row represents the inferior average spectra in frequencies: below 100 and above 100 Hz. The gray shaded areas represent the beta band (8–35 Hz), sHFO band (200–260 Hz), and fHFO band (260–400 Hz), respectively. (*C*) Boxplots demonstrating the subband power comparison between phenotypes in superior and inferior region. *Left* panel shows the distribution of beta-band power. *Right* panel shows the sHFO power in superior region and fHFO power in inferior region. The red lines indicate the group averages.

each depth indicated a strong interaction between the phase of beta oscillations and the amplitude of HFOs. However, the spatial localization of PAC was distinct. While PAC in TD subject was observed in the superior subregion, PIGD subject demonstrated PAC in the inferior subregion. Moreover, while the amplitude frequency of the coupling at the border was centered in the sHFO band, the PAC occurred at fHFO range in deeper segment. The average coupling in each group further supported our finding of spatially isolated PAC along with the distinct amplitude frequency components (Fig. 3*B*). The maximum PAC values obtained from the superior subregion were significantly higher in the TD group ($Z = 2.000$, $P = 0.023$, Mann–Whitney U test; Fig. 3*C*). Although both phenotypic groups exhibited fHFOs in the inferior subregion with significantly different peak frequencies, PAC analysis indicated a significantly higher coupling in the PIGD group ($Z = 1.877$, $P = 0.030$; Fig. 3*C*). In addition to the significantly higher PAC strength found in the superior subregion for TD and the inferior subregion for PIGD, the corresponding HFO (amplitude) frequencies were also at significantly different peaks ($Z = -2.857$, $P = 0.004$), indicating that amplitude modulation occurs at distinct frequencies in the TD and PIGD patients.

Discriminative and Predictive LFP Patterns. To show how well each of the features we studied can discriminate between subjects from TD and PIGD groups, we constructed receiver operator characteristic (ROC) curves. A point on the plot represents the sensitivity and specificity pair corresponding to a particular decision threshold. Consequently, if used for diagnosis, these ROC curves can provide an idea about how well one can distinguish between TD and PIGD patients. The ROC curves obtained from individual power of sHFO and fHFO bands and their ratio (sHFO/fHFO) computed in the STN subregions are shown in Fig. 4*A*. A statistically significant difference in sHFO/fHFO power ratio was observed between phenotypes only in the superior subregion (superior: $Z = 3.373$, $P = 0.001$; inferior: $Z = 1.674$, $P = 0.094$, Mann–Whitney U test; Fig. 4*B*). More importantly, this feature also provided the highest discrimination between phenotypes [area under curve (AUC) superior ratio, 0.89; inferior ratio, 0.69; superior sHFO, 0.77; inferior fHFO, 0.60].

To assess whether the spatiospectral features of LFPs were related to tremor or postural instability–gait and as well as akinetic-rigid symptoms of patients, a correlation analysis was performed. The correlation results between LFP features and UPDRS scores are provided in Table 1. We observed territorial

Telkes et al.

www.manaraa.com

NEUROSCIENCE
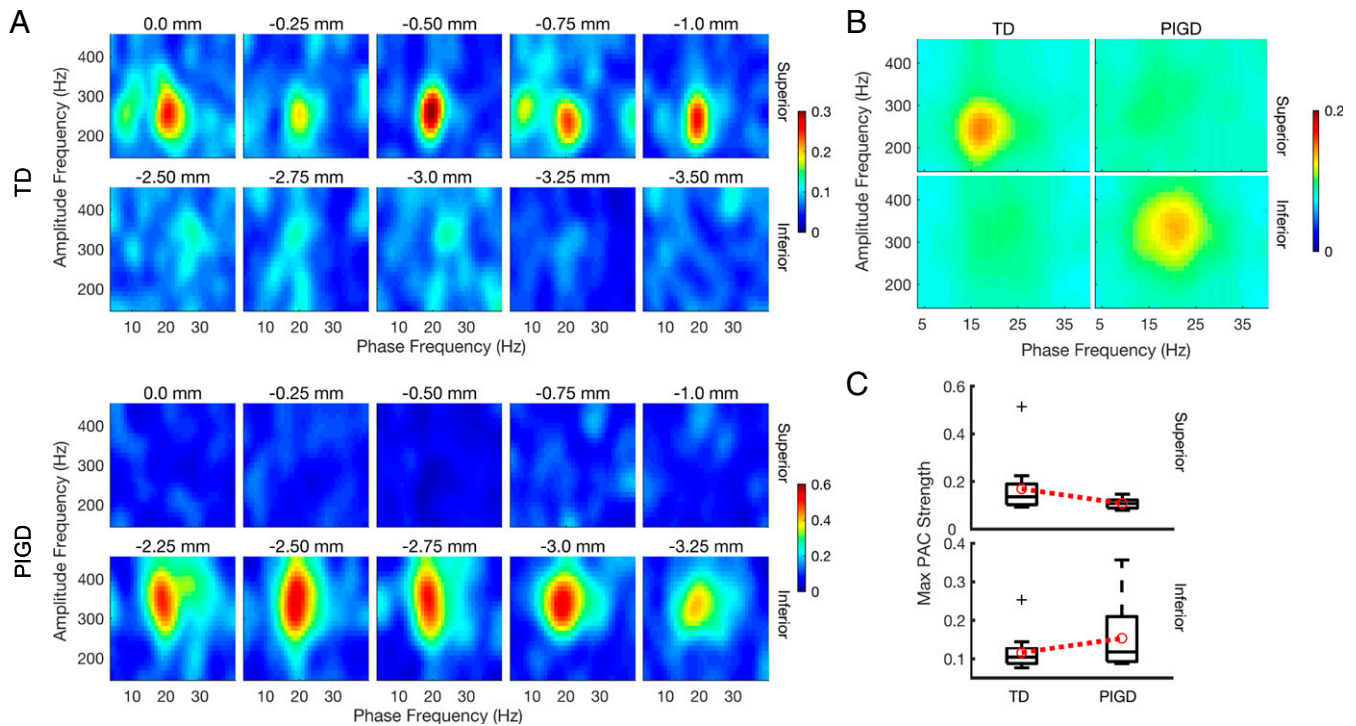
Fig. 3. PAC dynamics of LFPs in TD and PIGD groups. (*A*) PAC computed depth by depth is shown for a representative TD (*Top*) and a PIGD (*Bottom*) subject. *Upper* rows show the PAC in superior depths, while *Lower* rows show the PAC in inferior depths. Color bars indicate the PAC strength. (*B*) Average PAC in groups showing the spatial distribution of coupling between TD and PIGD. (*C*) Boxplots providing the spatial distribution of maximum PAC strength across phenotypes.

specificity in predicting the symptoms of patients. In particular, it was observed that sHFO/fHFO power ratio estimated from the superior region was positively correlated with the tremor ($r = 0.527$, $P = 0.008$) and negatively correlated with gait-related scores ($r = -0.586$, $P = 0.003$). Even though the HFO power ratio worked well for distinguishing between phenotypes, the ratio did not reflect a direct correlation to the level of severity of akinetic-rigid symptoms. Interestingly, the normalized beta-band power was correlated only with the akinetic-rigid symptoms and only at the deeper depths of the STN ($r = 0.505$, $P = 0.012$). The strength of beta-HFO PAC correlated with akinetic-rigid symptoms in the entire STN (superior: $r = 0.414$, $P = 0.044$; inferior: $r = 0.532$, $P = 0.008$) but not with the severity of tremor- or gait-related scores. (Also see *SI Appendix*, Note S2 and Fig. S2, Note S3 and Fig. S3, and Table S2.)

Discussion

Spatially and Phenotypically Localized sHFO in the STN. Microelectrode LFPs recorded from the subterritories of STN provide distinguishing information about the TD and PIGD phenotypes of PD. Our data demonstrate that TD and PIGD phenotypes are similar with respect to the energy of the beta band in the STN. However, a significant difference was seen in the energy of the higher frequencies and their nonlinear interaction with beta band within the STN. Specifically, compared with the PIGD group, LFPs of the TD group exhibited significantly stronger sHFO in the superior region closer to the entrance of STN. Both groups exhibited fHFOs in the inferior region further away from the STN entrance with slightly higher peak frequency in PIGD group, yet without any significant difference between their powers. The peak frequency of HFOs was found to be distinct in the subterritories of the STN and it was phenotype specific.

PAC Involved Different Frequency Components in the Subregions of STN. We also show a significantly stronger coupling between the phase of beta band and amplitude of sHFO in the superior re-

gion of STN in TD group. Although similar signal power was observed in fHFO range in the inferior subterritory of the STN in both groups, PAC between beta and fHFO was significantly stronger in the PIGD group. While nonlinear cross-frequency coupling (CFC) has been described as a physiological mechanism in memory circuits and sensory processing (19–22), the PAC patterns reported in STN (23) and cortex (24, 25) were linked to the pathophysiology of PD as levodopa administration and DBS resulted in symptom improvement and absence of PAC between beta band and HFOs range in STN-LFPs (23, 25, 26). Recently, it has been suggested that the consistent coupling between excessive beta band and HFOs could be impairing the rate coding in the basal ganglia–thalamocortical system (23). Given that
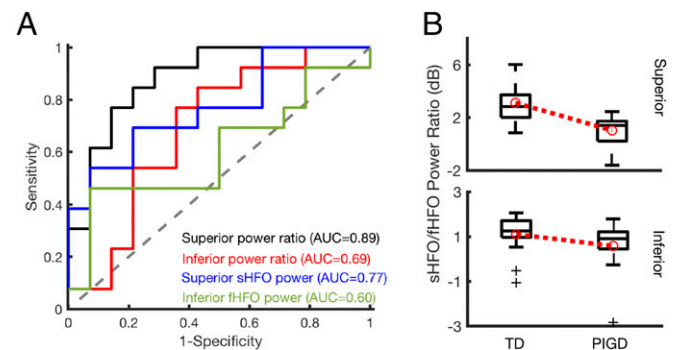
Fig. 4. Discriminative LFP patterns. (*A*) ROC curves discriminating TD from PIGD by using spatiospectral features of HFOs: superior sHFO/fHFO power ratio (black), inferior sHFO/fHFO power ratio (red), superior sHFO power (blue), and inferior fHFO power (green). AUC shows the discrimination power of the features. (*B*) Boxplots showing the sHFO/fHFO power ratio in superior and inferior regions of the STN between TD and PIGD. Red line points out the average ratio between groups.

Table 1. Correlation between "LFP features" and UPDRS subscores

Region	UPDRS items	Normalized beta power	sHFO/fHFO power ratio	Max PAC strength
Superior STN	Tr	$r = 0.120$	$r = 0.527$	$r = 0.245$
		$P = 0.575$	$P = 0.008$	$P = 0.248$
	Gait	$r = 0.028$	$r = -0.586$	$r = -0.248$
		$P = 0.898$	$P = 0.003$	$P = 0.243$
	BR	$r = 0.314$	$r = 0.012$	$r = 0.414$
		$P = 0.135$	$P = 0.955$	$P = 0.044$
Inferior STN	Tr	$r = 0.166$	$r = 0.278$	$r = -0.072$
		$P = 0.439$	$P = 0.189$	$P = 0.737$
	Gait	$r = 0.115$	$r = -0.271$	$r = 0.206$
		$P = 0.592$	$P = 0.201$	$P = 0.333$
	BR	$r = 0.505$	$r = 0.061$	$r = 0.532$
		$P = 0.012$	$P = 0.777$	$P = 0.008$

BR, mean scores of bilateral bradykinesia and rigidity in part III; Gait, mean gait-related scores including bilateral items in parts II–III; r, Spearman's correlation coefficient; Tr, mean tremor scores; UPDRS, Unified Parkinson's Disease Rating Scale. When parametric false-discovery rate (FDR) correction method was applied to these multicomparisons with a threshold of 0.05, the corrected P value was found to be 0.0081. The correlations that sustained the significance are marked in bold.

higher frequencies are used in DBS therapy, its therapeutic effect supports the hypothesis that DBS might be alleviating the PD symptoms by mimicking the HFO rhythms (27, 28). Consequently, one could further speculate that the suppression of beta-band oscillations might be also related to the effects of DBS at HFO bands.

Earlier studies have shown PAC in motor cortex between beta phase and broadband gamma (50–200 Hz) amplitude (24). However, the latest research challenged these PAC patterns reported in motor cortex and suggested that this coupling could have originated from the harmonics of the nonsinusoidal beta-band activity (29, 30). The broadband activity arises from the sharp-edged beta waveforms in the time domain and includes high-frequency broadband harmonic components in the frequency domain. These broadband harmonics produce spurious CFC, even when a true physiological interaction is absent. However, in our recordings, the HFO activity did not appear as a broadband signal. Both sHFO and fHFO were band limited and had a clear peak. Moreover, the comodulograms we estimated show that the coupling occurs between well-localized beta and high-frequency components not in broadband form. These observations suggest that our CFC patterns are a result of well-localized frequency components not due to harmonics of nonsinusoidal low-band activity with a spectral leakage into higher frequencies.

Spatiospectral Features of LFPs Correlated with UPDRS Scores. We observed that spatiospectral features could discriminate the clinically identified groups and be correlated with the symptoms of the patients with territorial specificity. In particular, the sHFO/fHFO features derived from the superior border of STN provided best discrimination between TD and PIGD groups and were significantly correlated with tremor and gait-related scores of patients but not bradykinesia plus rigidity. Interestingly, the beta-band power of the inferior region and the beta-HFO PAC obtained from both superior and inferior regions were significantly correlated with bradykinesia plus rigidity but not with tremor and gait-related scores. Our results confirm the previous findings of significant correlation between beta-band power and akinetic-rigid symptoms estimated in OFF state (26, 31, 32). Others have found this relation only between the ratio of beta-band power suppression and the improvement of akinetic-rigid

symptoms following administration of dopaminergic medication (33, 34).

We acknowledge that, using macroelectrode LFPs, a significant correlation was previously shown between sHFO/fHFO power ratio and tremor during resting state by Hirschmann et al. (35). To our knowledge, a correlation between microelectrode LFP patterns and tremor and gait scores has not been reported. The novelty of our study is the spatial investigation of sHFO/fHFO power ratio across the STN and its differential correlations with both tremor and gait at resting state. The assessment of LFPs and its high-frequency components were previously studied using macroelectrodes (23, 26, 27, 35). The standard DBS leads with 1.5-mm contact width, 1.27-mm outer diameter, and 2-mm center-to-center distance (model 3389; Medtronic) have a lower spatial resolution than the microelectrodes used in this study (NeuroProbe; AlphaOmega), which have 1-mm contact size and 0.7-mm outer diameter. Given the 4- to 6-mm dorsal-to-ventral span of the STN, it is possible that LFPs obtained from DBS leads with bipolar configuration might represent oscillations from more than one territory. Therefore, scanning subthalamic oscillations with a finer spatial resolution and depth by depth likely provides a better understanding about their territorial characteristic.

Possible Multiscale Origins of Electrophysiological Footprints of PD Phenotypes. Somatotopic organization of STN through single-cell recordings is well established. Many groups consistently reported that most of the single neuronal firings related to upper and lower limb movements were located in the dorsolateral region of STN, which appears to be the most clinically effective target for high-frequency stimulation (36–41). Previous studies also suggest that beta oscillating units are more commonly found at the dorsolateral aspect of the STN (36, 42), while gamma activities are stronger in more ventral areas (43). More importantly, tremor-related neurons were repeatedly captured in the dorsolateral STN (36, 44, 45) as opposed to the ventral parts and stimulation of these sites induced tremor arrest (36). A recent study examined the location of STN units and their correlation with PD symptoms including bradykinesia, rigidity, and axial scores (46) and observed that beta oscillating units were significantly closer to the upper border of the STN (<1.5 mm) than nonoscillating units and that these beta units were strongly correlated with rigidity. In contrast, gamma oscillating units appeared to be more common in the medial STN and strongly correlated with bradykinesia. Finally, units with subbeta power were located significantly further from the upper STN border and were strongly correlated with axial scores. These findings suggest that there are cells with distinct firing characteristic in the territories of STN that individually correlate with the cardinal motor symptoms of PD. From a somatotopic perspective, the sHFO that we located within 1.5–2 mm from the superior border of the STN correlates with the spatially segregated tremorous single-cell activity and movement cells. Compared with sHFOs, the fHFOs in the PIGD group start at deeper segments following the STN entrance. The location of these oscillations is overlapping with the location of the cells predicting the axial symptoms of patients (46) and with the ones with faster firing characteristic in the gamma range (43).

Little is known about the cellular and network mechanism of HFOs in the STN. As in the gamma band, the amplitude of HFO increases with movement (26, 27). Previously, the existence of fHFO was reported only in ON medication state (23, 26) or a shift from sHFO to fHFO range was observed in those PD patients after administration of dopaminergic medication (23, 26, 27). Here, we show that even though the recordings were obtained during medication OFF state, the fHFOs can also be observed in the STN. It is also possible to observe HFOs at different frequencies in distinct territories of STN in the same patient.

NEUROSCIENCE

Interestingly, HFOs between 80–600 Hz are also reported in epileptogenic brain regions of humans and rodents (47, 48), and they have been linked to the pathological hypersynchronous bursting pattern of a small population of neurons (49). One recent study has suggested that HFOs can arise both from in-phase and out-of-phase firing of neurons in the epileptic hippocampus (50). While in-phase firing produces pure oscillations that can reach frequencies up to 300 Hz, the organization of out-of-phase firing produces emergent oscillations at even higher frequencies from slower-discharging cells. Given that the bursting firing pattern in basal ganglia nuclei was commonly reported in PD patients (51, 52) and animal models/nonhuman primates (53, 54), the sHFOs and fHFOs in the different segments of STN could originate from these in- and out-of-phase bursting firing of cell populations or microcircuits involving such populations.

In this study, we could not see any difference in beta power at superior and inferior regions, indicating that the beta band is widely distributed in the STN. sHFOs are frequently captured in the more dorsal contacts of the DBS electrodes (26, 55, 56). We have previously shown that the HFOs that are located at the dorsal contacts of the DBS electrode are modulated with the beta band captured from both dorsal and ventral contacts that are several millimeters away (55). These findings suggest that HFOs are indeed more focally located as others have also reported (57) and the beta band is widely distributed within the STN. To our knowledge, only one study (58) explored HFOs and single-cell firings jointly with the beta oscillations in STN and found that both the amplitude of HFOs and single-cell firing were significantly coupled to the phase of beta oscillations. Both couplings showed a similar spatial topography: PAC and spike-phase locking were most pronounced near the superior border of the STN. Interestingly, one recent study also showed that the STN cell firings in PD patients were phase synchronized to both low– and high–beta-frequency cortical oscillations (59). Furthermore, this relationship was not exclusive to motor cortex, as they show the STN firing also demonstrated phase synchronization to both premotor and sensory cortex. Based on these observations, the excessive beta oscillations seem to be a common activity in cortico-basal ganglia loop involved in neural communication and HFOs are likely a result of pathological microcircuits in STN that represent the activity of a population of neurons.

It has been hypothesized that the exaggerated PAC might hamper neural processing where too much synchrony consumes an excessive amount of "neural bandwidth" (60–63). This hypothesis implies that excessive beta oscillations in STN modulating the amplitude of HFOs and rate of single-cell firings in different territories yields an exaggerated neuronal synchrony, which interferes with the information that can be transmitted by neuronal ensembles in this nucleus (64) and could be impairing the rate coding in the basal ganglia–thalamocortical system (23). In vivo studies have demonstrated that the stimulation-induced activity of STN neurons is transmitted to other nuclei such as globus pallidus internus (GPi), globus pallidus externus (GPe), and substantia nigra reticulata (SNr) through projections (65–67). STN also receives input from primary and somatosensory motor cortex, pre- and supplementary motor areas, thalamus, and pedunculopontine nucleus (PPN) (68). Consequently, it is likely that the level of dopamine depletion in the territories of STN or other structures might have increased the pathologic synchronization in basal ganglia–cortical loop through their reciprocal projections. It is likely that cerebello-thalamo-cortical circuits contribute to the generation of parkinsonian symptoms through these projections as high-frequency stimulation or lesioning different nodes throughout this network [including STN, GPi, ventral intermediate nucleus (Vim), and PPN] can suppress parkinsonian symptoms (69–72) by breaking or regularizing the loop. Thus, both the intrinsic properties of subthalamic neurons, biased dopamine depletion in the territories of

basal ganglia nuclei, phenotypic functional connectivity, and the involvement of the STN in cortico-subcortical loops argue for a fundamental contribution to the electrophysiological differences that we observed between phenotypes in the current study.

Conclusions

In summary, we have shown that spatiospectral patterns and cross-frequency interactions of LFPs carry substantial information that can distinguish between PD motor subtypes. As recently as 2013, an international survey of high-volume DBS implanting sites revealed that 83% of centers used microelectrode recording for the placement of DBS electrodes (73). LFPs are more robust signals than single-cell activity recorded from a high-impedance microelectrode tip, and the former are particularly sensitive to synchronous and oscillatory firing patterns (74, 75). LFPs have also been shown to be better correlated with motor and non-motor symptoms of PD (75, 76). In our recent study, we have shown that microelectrode LFPs measured intraoperatively can also be used for the localization of STN for DBS electrode implantation (77). There has been growing interest over the last decade in the development of segmented chronic electrodes with smaller contact sizes (higher spatial resolution) to deliver directional stimulation, to provide more selected modulation and reduce the side effects of DBS (78–80). By demonstrating the feasibility of using microelectrode LFPs for identification of physiological signatures of PD subtypes, our findings can guide identification of STN subterritories that are responsible for the manifestation of phenotypic symptoms. Given that recent advances in implantable pulse generator technology allows to record LFP activity from chronically implanted DBS electrodes (81, 82), one can isolate these territories with focal sensing and then deliver targeted stimulation (current steering) to personalize DBS therapy. For instance, based on the distribution of HFOs and PAC patterns, a subset of electrode contacts could be selected for delivery of stimulation to these specific territories. This might also help with the reduction of side effects.

Our study provides a rationale for future research into individualized DBS targeting within the subterritories of STN using lead designs and/or stimulation strategies. In addition, chronic studies are needed to assess the value of identified neural patterns in predicting the phenotypic symptoms and their response to DBS.

Materials and Methods

Patients. This was a two-center study in which patients were recruited either at Baylor College of Medicine or Fairview Hospital of the University of Minnesota. The experimental protocol was approved by the Institutional Review Boards of the University of Minnesota, University of Houston, and Baylor College of Medicine. All patients provided written informed consent for study participation. Intraoperative LFPs were recorded from 24 patients (7 women, 17 men) who were diagnosed with idiopathic PD. Patients included in this study exhibited typical motor symptoms, including tremor, rigidity, bradykinesia, and PIGD. Patients were clinically evaluated by a movement disorder specialist, and either UPDRS or MDS-UPDRS scores were obtained in the OFF- and ON-medication states 4.2 ± 2.5 mo before the DBS surgery. To designate the motor phenotypes of the patients, tremor scores and gait-related scores of UPDRS or MDS-UPDRS were used with the formula suggested by Jankovic et al. (5, 7). Patients with a ratio of mean tremor scores to mean gait-related scores larger than or equal to 1.5 were assigned to TD group. The patients with a ratio less than or equal to 1 were assigned to PIGD group and those patients between 1 and 1.5 were excluded from the study as they fall in the mixed group (additional data and analysis results related to three patients with mixed subtype are provided in *SI Appendix*). Clinical characteristics of included subjects are provided in *SI Appendix*, Table S1.

Surgical Procedure. Surgeries were performed in awake patients using local anesthesia. Patients were asked to discontinue Parkinson's medications 24 h before DBS surgery. The radiological coordinates and trajectories to the STN were identified by fusing preoperative stereotactic MRIs to a preoperative or an intraoperative stereotactic computed tomography scan on

a neuro-navigational platform (StealthStation; Medtronic). This radiographic target was refined using electrophysiological recordings from three parallel track microelectrodes (NeuroProbe; AlphaOmega) to identify single-cell and LFP characteristics of the STN, as per standard clinical protocol (Fig. 5 A and B). In all patients, tracks targeting the STN in the hemisphere contralateral to the dominant motor symptoms were used. Starting from maximum 25 mm above the radiographic target, at least 30 s of baseline recordings were obtained at each depth until one of the microelectrode tips had first passed through the superior and then the inferior border of STN. Electrodes were moved initially using a 1-mm step size. Within 5 mm of the radiographic target, the step size was reduced to 0.5 or 0.25 mm to allow more precise identification of the STN borders. The location of the dorsal entry and ventral exit from the STN was determined by an experienced clinical neurophysiologist through listening to and visually observing the microelectrode recording of single-unit activities (MER-SUAs). As others did (57, 58), the dorsal border of STN is detected when a prominent increase in background activity or uniform firing characteristic of border cells are observed. The location of the dorsal border of STN is used as reference depth (0 mm), and the characteristics of LFP patterns in superior and inferior regions of STN are reported in terms of relative distance to the border (Fig. 5C). Along with resting-state single-unit and LFP activity obtained through the microelectrode, we simultaneously recorded high-definition video and other biosignals, such as EMG, ECG, and accelerometer signals with a bioamplifier (Grapevine Neural Interface and Processor; Ripple) at 2 kHz and 16-bit A/D resolution.

Data Analysis. All data were visualized and analyzed off-line with a custom in-house developed software (83) in Matlab 2014a (Mathworks). Based on video and EMG, the data were annotated and resting-state segments were extracted at each depth for further analysis.

Spatial projection. Three simultaneous microelectrode trajectories separated by 2 mm from central axis to axis (Fig. 5A) were selected for each patient based on stereotaxic imaging. When microelectrodes enter the STN, an excessive oscillatory activity is observed. However, these oscillations appeared at different tracks in each patient. To fuse information from multiple electrode tracks, reduce variability among patients, and increase the signal-to-noise ratio compared with the original signals in each individual trajectory, a spatial projection based on the weighted linear combination of LFPs from three tracks was utilized (Fig. 6A). More specifically, artifact-free LFP data in each trajectory were divided into two groups: (*i*) LFP data recorded from those depths at which the electrodes were determined to be in the STN, and (*ii*) LFP data recorded between superior border of STN and 5 mm above it, which were used as baseline. LFP signals at these depths were filtered between 4- and 450-Hz cutoff frequencies by using a fifth-order Butter-

worth filter. Then, 3×3 spatial covariance matrices, $\sum_{STN}$ and $\sum_{Base}$, were calculated using the LFP data from three tracks. Using objective function (Eq. **1**),

$$\lambda = \frac{\omega^T \sum_{STN} \omega}{\omega^T \sum_{Base} \omega},$$ [1]

we searched for a spatial projection vector, ω, to maximize the variance ratio, λ. This is a generalized eigenvalue decomposition (GED) problem and the eigenvector corresponding to the largest eigenvalue was chosen to maximize λ. Ultimately, three-track LFP data at each depth were projected into a single virtual channel using this eigenvector ω, which combines the recordings in a linear weighted fashion (Fig. 6A). This projection was executed in each case to adapt trajectory differences across subjects and simply fused information from multiple electrode tracks. The projected data were used in the further analysis for feature extraction and to investigate the spatio-spectral dynamics of the LFPs in each phenotype.

Spectral analysis. To visualize and study the depth-varying spectral dynamics, a modified Welch periodogram method with robust statistics was used to map the projected LFP data to the frequency domain at each depth (77). A fast Fourier transform was computed with a 1-s Hanning window, and the window was shifted with 50% overlap. A median spectrum was calculated from the spectra to eliminate localized artifacts at each depth. Then, individual spectra across depths were combined to generate a 2D DFM showing the depth-varying power spectrum of the LFPs, with the y axis representing depth and the x axis representing frequency (Fig. 6B). Each map was resampled with a 0.25-mm depth resolution and cubic interpolation to obtain equidistant depth values. A Gaussian kernel filter was used to smooth the maps. DFMs were then aligned according to the dorsal border of the STN, which was identified in each case based on MER-SUA. In these maps, 0 mm was used to signify the superior border of the STN in all subjects. In addition to individual maps, all DFMs were averaged independent of the patient's phenotypic designation, and a global baseline spectrum with minimum power was calculated above the superior border. Then, individual DFMs of TD and PIGD subjects were separated, and a single map was generated for each phenotype by intragroup averaging. These two maps were normalized according to Eq. **2** by previously extracted baseline spectrum and are shown in decibel scale,

$$n_{dfm} = 20 \times \log_{10}\left(\frac{r_{dfm}}{base}\right),$$ [2]

where n_{dfm} is the normalized DFM in decibel scale, r_{dfm} is the raw DFM, and the *base* is the baseline spectrum.

Visualization of DFMs revealed localized sHFOs and fHFOs (150–450 Hz) in the territories of STN. To further characterize these focal activities, from the average DFM, the peak frequency between 150 and 450 Hz at each depth was obtained starting from the superior border until the final depth. Then, STN was divided into superior and inferior regions based on the shift in peak frequency of HFOs. This segmentation was applied to all subjects. The rest of the analyses were then individually computed in these defined segments to explore the spectral dynamics of LFPs in the superior and inferior regions of the STN (Fig. 6B).

Subband features. An average LFP power spectrum was computed within the superior and inferior regions in each subject (Fig. 6C). Additionally, a baseline power spectrum was computed from the LFP data recorded between superior border of STN and 5 mm above it. In total, three spectra representing baseline (out of STN), superior STN, and inferior STN segments were derived per subject. The beta-band range was defined as 8–35 Hz. The lower- and upper-frequency limits for subband features in HFO range were determined according to visual inspection of the average spectra in groups without any normalization. sHFO range was defined from 200 to 260 Hz (due to a sharp peak in the superior STN region in the TD group), and a fHFO range was defined from 260 to 400 Hz. Subband powers in the beta, sHFO, and fHFO frequency bands were computed in the superior and inferior STN regions and normalized to the baseline power and converted to decibel scale, representing the relative in-STN power change in different subterritories.

PAC. PAC for nonlinear interactions between the phase of beta and amplitude of HFO bands was investigated by using a phase-locking value (PLV) approach (84). We investigated the 150- to 450-Hz range as amplitude frequencies. The frequency band ranging from 4 to 40 Hz was investigated as phase frequencies. LFP data were bandpass filtered with a third-order Butterworth filter from 4 to 40 Hz with a 2-Hz bandwidth and 1-Hz shift. The same LFPs were filtered between 150 and 450 Hz in the HFO range with a 50-Hz bandwidth and 12.5-Hz shift using a third-order Butterworth filter. The envelope of HFOs was computed by using the Hilbert transform, and PLV
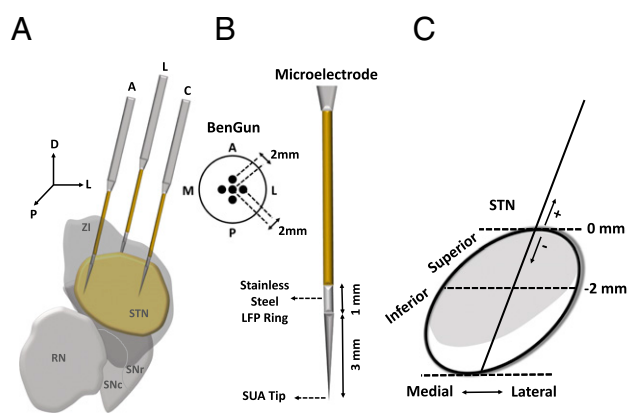
Fig. 5. Representation of LFP recordings from STN by using multiple microelectrodes. (*A*) Three-dimensional representation of three-track microelectrode implantation into STN through five-hole BenGun. A, anterior; C, center; L, lateral; M, medial; and P, posterior trajectory. (*B*) Schematic of a routinely used AlphaOmega recording microelectrode with a microrecording tip and a 1-mm-wide stainless-steel (SS) contact situated 3 mm proximal to this tip. LFPs were recorded from the SS ring of the electrode. (*C*) Schematic representation of STN from coronal view and the trajectory of an optimally placed microelectrode. Black dashed lines from *Top* to *Bottom* indicate the superior STN border, separation line dividing STN into superior and inferior subregions, and the inferior border of STN. Gray shaded area represents the motor STN.

Telkes et al.

www.manaraa.com
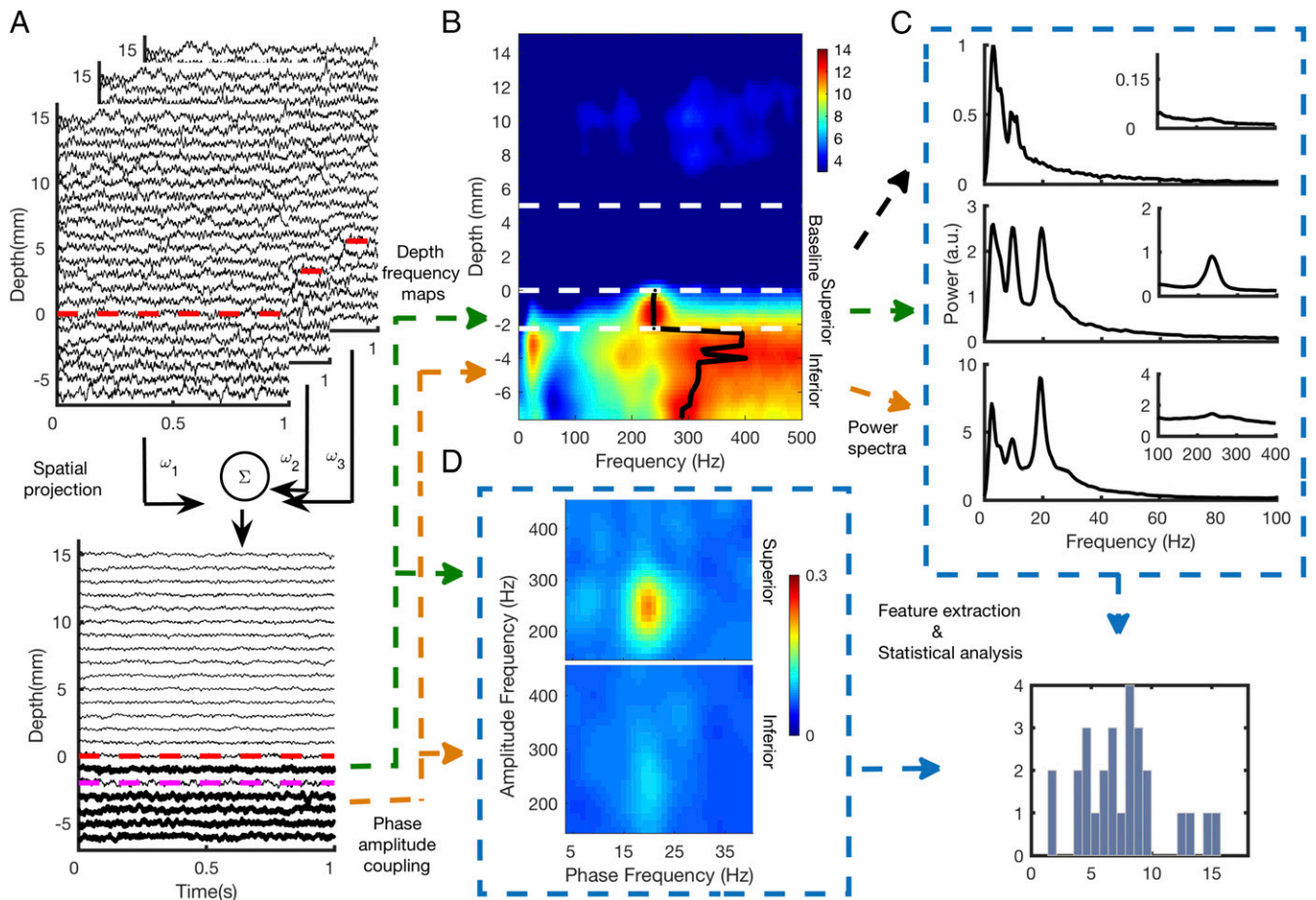
Fig. 6. Schematic diagram representing the workflow. (*A*) Raw LFPs recorded intraoperatively from SS contacts are shown along with calculated spatial projection vectors. By using a GED technique, multiple channels were converted to single channel by preserving depth-specific information. Projected LFPs are shown depth by depth, and the superior STN border, which was determined by neurosurgeon and/or neurologist in the operating room, was marked with red dashed line at depth 0 mm. (*B*) A typical example of DFM of a TD subject. It demonstrates the spatially localized sHFOs with 2-mm span just after the intraoperatively determined superior border of STN. Black line indicates the peak frequency found between 150 and 450 Hz in each depth and clearly shows the depth (2 mm) of frequency shift. Due to this consistent shift in TD group, STN was divided into superior and inferior segments as shown in-between the white dashed lines. The *Top* line indicates the border of baseline above the STN, which was used for normalization. (*C*) Average power spectrum obtained from each segment shown in *B*. Superior and inferior region spectra were computed by averaging individual spectrum in each depth, while baseline spectrum was calculated by finding minimum power spectrum across depths of out-STN. (*D*) Comodulogram of PAC of the same TD subject. The *x* axis shows the phase frequency, and the *y* axis shows the amplitude frequency.

was calculated for all combinations and displayed in a representative comodulogram for each depth in the STN. Comodulograms in the superior and inferior subterritories were computed and the maximum PAC strength (values between 0 and 1) was extracted in each subject (Fig. 6*D*).

Statistics. Statistical analyses were also performed in Matlab 2014a. To assess the normality and the homogeneity assumptions of Student's *t* test for the feature distribution, the Shapiro–Wilk test and Levene's test were used, respectively. However, assumptions were not held for most of the variables. Therefore, the nonparametric Mann–Whitney *U* test for unpaired samples and the Wilcoxon signed-rank test for paired samples were used. The Mann–Whitney *U* test was applied to compare the spectral features and the maximum PAC strength between phenotypes. For the intragroup comparisons of

the spectral features obtained from the same region, the Wilcoxon signed-rank test was used. The significance threshold was set to 0.05 in all of the statistical analyses.

The ROC curves were generated for extracted features and the area under the ROC curve (AUC) was used to quantify the discrimination power of features between phenotypes. To quantify the correlation between LFP features and the tremor and gait-related scores, Spearman's correlation analysis was used.

1. Thenganatt MA, Jankovic J (2014) Parkinson disease subtypes. *JAMA Neurol* 71: 499–504.
2. Graham JM, Sagar HJ (1999) A data-driven approach to the study of heterogeneity in idiopathic Parkinson's disease: Identification of three distinct subtypes. *Mov Disord* 14:10–20.
3. Lewis SJG, et al. (2005) Heterogeneity of Parkinson's disease in the early clinical stages using a data driven approach. *J Neurol Neurosurg Psychiatry* 76:343–348.
4. Selikhova M, et al. (2009) A clinico-pathological study of subtypes in Parkinson's disease. *Brain* 132:2947–2957.
5. Jankovic J, et al.; The Parkinson Study Group (1990) Variable expression of Parkinson's disease: A base-line analysis of the DATATOP cohort. *Neurology* 40:1529–1534.
6. Nutt JG (2016) Motor subtype in Parkinson's disease: Different disorders or different stages of disease? *Mov Disord* 31:957–961.
7. Stebbins GT, et al. (2013) How to identify tremor dominant and postural instability/gait difficulty groups with the movement disorder society unified Parkinson's disease rating scale: Comparison with the unified Parkinson's disease rating scale. *Mov Disord* 28:668–670.
8. Alves G, Larsen JP, Emre M, Wentzel-Larsen T, Aarsland D (2006) Changes in motor subtype and risk for incident dementia in Parkinson's disease. *Mov Disord* 21:1123–1130.
9. Skeie GO, Muller B, Haugarvoll K, Larsen JP, Tysnes OB (2010) Differential effect of environmental risk factors on postural instability gait difficulties and tremor dominant Parkinson's disease. *Mov Disord* 25:1847–1852.

www.manaraa.com

10. Herman T, et al. (2013) White matter hyperintensities in Parkinson's disease: Do they explain the disparity between the postural instability gait difficulty and tremor dominant subtypes? *PLoS One* 8:e55193.

11. Katz M, et al.; CSP 468 Study Group (2015) Differential effects of deep brain stimulation target on motor subtypes in Parkinson's disease. *Ann Neurol* 77:710–719.

12. Jankovic J, Kapadia AS (2001) Functional decline in Parkinson disease. *Arch Neurol* 58: 1611–1615.

13. Halliday GM, McCann H (2010) The progression of pathology in Parkinson's disease. *Ann N Y Acad Sci* 1184:188–195.

14. Marras C, Lang A (2013) Parkinson's disease subtypes: Lost in translation? *J Neurol Neurosurg Psychiatry* 84:409–415.

15. Schiess MC, Zheng H, Soukup VM, Bonnen JG, Nauta HJW (2000) Parkinson's disease subtypes: Clinical classification and ventricular cerebrospinal fluid analysis. *Parkinsonism Relat Disord* 6:69–76.

16. Rossi C, et al. (2010) Differences in nigro-striatal impairment in clinical variants of early Parkinson's disease: Evidence from a FP-CIT SPECT study. *Eur J Neurol* 17:626–630.

17. Eggers C, Kahraman D, Fink GR, Schmidt M, Timmermann L (2011) Akinetic-rigid and tremor-dominant Parkinson's disease patients show different patterns of FP-CIT single photon emission computed tomography. *Mov Disord* 26:416–423.

18. Lewis MM, et al. (2011) Differential involvement of striato- and cerebello-thalamo-cortical pathways in tremor- and akinetic/rigid-predominant Parkinson's disease. *Neuroscience* 177:230–239.

19. Canolty RT, et al. (2010) Oscillatory phase coupling coordinates anatomically dispersed functional cell assemblies. *Proc Natl Acad Sci USA* 107:17356–17361.

20. Lakatos P, Karmos G, Mehta AD, Ulbert I, Schroeder CE (2008) Entrainment of neuronal oscillations as a mechanism of attentional selection. *Science* 320:110–113.

21. Tort AB, et al. (2008) Dynamic cross-frequency couplings of local field potential oscillations in rat striatum and hippocampus during performance of a T-maze task. *Proc Natl Acad Sci USA* 105:20517–20522.

22. Cohen MX, et al. (2009) Good vibrations: Cross-frequency coupling in the human nucleus accumbens during reward processing. *J Cogn Neurosci* 21:875–889.

23. Özkurt TE, et al. (2011) High frequency oscillations in the subthalamic nucleus: A neurophysiological marker of the motor state in Parkinson's disease. *Exp Neurol* 229: 324–331.

24. de Hemptinne C, et al. (2013) Exaggerated phase-amplitude coupling in the primary motor cortex in Parkinson disease. *Proc Natl Acad Sci USA* 110:4780–4785.

25. de Hemptinne C, et al. (2015) Therapeutic deep brain stimulation reduces cortical phase-amplitude coupling in Parkinson's disease. *Nat Neurosci* 18:779–786.

26. López-Azcárate J, et al. (2010) Coupling between beta and high-frequency activity in the human subthalamic nucleus may be a pathophysiological mechanism in Parkinson's disease. *J Neurosci* 30:6667–6677.

27. Foffani G, et al. (2003) 300-Hz subthalamic oscillations in Parkinson's disease. *Brain* 126:2153–2163.

28. Foffani G, Priori A (2006) Deep brain stimulation in Parkinson's disease can mimic the 300 Hz subthalamic rhythm. *Brain* 129:e59; author reply e60.

29. Cole SR, et al. (2017) Nonsinusoidal beta oscillations reflect cortical pathophysiology in Parkinson's disease. *J Neurosci* 37:4830–4840.

30. Lozano-Soldevilla D, Ter Huurne N, Oostenveld R (2016) Neuronal oscillations with non-sinusoidal morphology produce spurious phase-to-amplitude coupling and directionality. *Front Comput Neurosci* 10:87.

31. Kühn AA, et al. (2009) Pathological synchronisation in the subthalamic nucleus of patients with Parkinson's disease relates to both bradykinesia and rigidity. *Exp Neurol* 215:380–387.

32. van Wijk BC, et al. (2016) Subthalamic nucleus phase-amplitude coupling correlates with motor impairment in Parkinson's disease. *Clin Neurophysiol* 127:2010–2019.

33. Kühn AA, Kupsch A, Schneider GH, Brown P (2006) Reduction in subthalamic 8–35 Hz oscillatory activity correlates with clinical improvement in Parkinson's disease. *Eur J Neurosci* 23:1956–1960.

34. Ray NJ, et al. (2008) Local field potential beta activity in the subthalamic nucleus of patients with Parkinson's disease is associated with improvements in bradykinesia after dopamine and deep brain stimulation. *Exp Neurol* 213:108–113.

35. Hirschmann J, et al. (2016) Parkinsonian rest tremor is associated with modulations of subthalamic high-frequency oscillations. *Mov Disord* 31:1551–1559.

36. Rodriguez-Oroz MC, et al. (2001) The subthalamic nucleus in Parkinson's disease: Somatotopic organization and physiological characteristics. *Brain* 124:1777–1790.

37. Abosch A, Hutchison WD, Saint-Cyr JA, Dostrovsky JO, Lozano AM (2002) Movement-related neurons of the subthalamic nucleus in patients with Parkinson disease. *J Neurosurg* 97:1167–1172.

38. Lanotte MM, et al. (2002) Deep brain stimulation of the subthalamic nucleus: Anatomical, neurophysiological, and outcome correlations with the effects of stimulation. *J Neurol Neurosurg Psychiatry* 72:53–58.

39. Saint-Cyr JA, et al. (2002) Localization of clinically effective stimulating electrodes in the human subthalamic nucleus on magnetic resonance imaging. *J Neurosurg* 97: 1152–1166.

40. Starr PA, et al. (2002) Implantation of deep brain stimulators into the subthalamic nucleus: Technical approach and magnetic resonance imaging-verified lead locations. *J Neurosurg* 97:370–387.

41. Theodosopoulos PV, Marks WJ, Jr, Christine C, Starr PA (2003) Locations of movement-related cells in the human subthalamic nucleus in Parkinson's disease. *Mov Disord* 18:791–798.

42. Weinberger M, et al. (2006) Beta oscillatory activity in the subthalamic nucleus and its relation to dopaminergic response in Parkinson's disease. *J Neurophysiol* 96: 3248–3256.

43. Zaidel A, Spivak A, Grieb B, Bergman H, Israel Z (2010) Subthalamic span of β oscillations predicts deep brain stimulation efficacy for patients with Parkinson's disease. *Brain* 133:2007–2021.

44. Amtage F, et al. (2008) Tremor-correlated neuronal activity in the subthalamic nucleus of Parkinsonian patients. *Neurosci Lett* 442:195–199.

45. Amtage F, et al. (2009) High functional connectivity of tremor related subthalamic neurons in Parkinson's disease. *Clin Neurophysiol* 120:1755–1761.

46. Sharott A, et al. (2014) Activity parameters of subthalamic nucleus neurons selectively predict motor symptom severity in Parkinson's disease. *J Neurosci* 34:6273–6285.

47. Worrell GA, et al. (2008) High-frequency oscillations in human temporal lobe: Simultaneous microwire and clinical macroelectrode recordings. *Brain* 131:928–937.

48. Bragin A, Engel J, Wilson CL, Fried I, Mathern GW (1999) Hippocampal and entorhinal cortex high-frequency oscillations (100–500 Hz) in human epileptic brain and in kainic acid-treated rats with chronic seizures. *Epilepsia* 40:127–137.

49. Bragin A, Wilson CL, Engel J, Jr (2000) Chronic epileptogenesis requires development of a network of pathologically interconnected neuron clusters: A hypothesis. *Epilepsia* 41(Suppl 6):S144–S152.

50. Ibarz JM, Foffani G, Cid E, Inostroza M, Menendez de la Prida L (2010) Emergent dynamics of fast ripples in the epileptic hippocampus. *J Neurosci* 30:16249–16261.

51. Gale JT, Shields DC, Jain FA, Amirnovin R, Eskandar EN (2009) Subthalamic nucleus discharge patterns during movement in the normal monkey and Parkinsonian patient. *Brain Res* 1260:15–23.

52. Starr PA, et al. (2005) Spontaneous pallidal neuronal activity in human dystonia: Comparison with Parkinson's disease and normal macaque. *J Neurophysiol* 93:3165–3176.

53. Bergman H, Wichmann T, Karmon B, DeLong MR (1994) The primate subthalamic nucleus. II. Neuronal activity in the MPTP model of parkinsonism. *J Neurophysiol* 72: 507–520.

54. Wichmann T, Soares J (2006) Neuronal firing before and after burst discharges in the monkey basal ganglia is predictably patterned in the normal state and altered in parkinsonism. *J Neurophysiol* 95:2120–2133.

55. Meloni G, Sen A, Abosch A, Ince NF (2015) Spatial distribution of nonlinear interactions in subthalamic nucleus local field potentials in Parkinson's disease. 2015 37th Annual International Conference of the IEEE *Engineering in Medicine and Biology Society (EMBC)* (Institute of Electrical and Electronics Engineers, Piscataway, NJ), pp 5557–5560.

56. van Wijk BCM, et al. (2017) Localization of beta and high-frequency oscillations within the subthalamic nucleus region. *Neuroimage Clin* 16:175–183.

57. Wang J, et al. (2014) High-frequency oscillations in Parkinson's disease: Spatial distribution and clinical relevance. *Mov Disord* 29:1265–1272.

58. Yang AI, Vanegas N, Lungu C, Zaghloul KA (2014) Beta-coupled high-frequency activity and beta-locked neuronal spiking in the subthalamic nucleus of Parkinson's disease. *J Neurosci* 34:12816–12827.

59. Lipski WJ, et al. (2017) Dynamics of human subthalamic neuron phase-locking to motor and sensory cortical oscillations during movement. *J Neurophysiol* 118: 1472–1487.

60. Reyes AD (2003) Synchrony-dependent propagation of firing rate in iteratively constructed networks in vitro. *Nat Neurosci* 6:593–599.

61. Rossant C, Leijon S, Magnusson AK, Brette R (2011) Sensitivity of noisy neurons to coincident inputs. *J Neurosci* 31:17193–17206.

62. Brette R (2012) Computing with neural synchrony. *PLoS Comput Biol* 8:e1002561.

63. Börgers C, Li J, Kopell N (2014) Approximate, not perfect synchrony maximizes the downstream effectiveness of excitatory neuronal ensembles. *J Math Neurosci* 4:10.

64. Averbeck BB, Latham PE, Pouget A (2006) Neural correlations, population coding and computation. *Nat Rev Neurosci* 7:358–366.

65. Hashimoto T, Elder CM, Okun MS, Patrick SK, Vitek JL (2003) Stimulation of the subthalamic nucleus changes the firing pattern of pallidal neurons. *J Neurosci* 23: 1916–1923.

66. Degos B, et al. (2005) Neuroleptic-induced catalepsy: Electrophysiological mechanisms of functional recovery induced by high-frequency stimulation of the subthalamic nucleus. *J Neurosci* 25:7687–7696.

67. Maurice N, Thierry AM, Glowinski J, Deniau JM (2003) Spontaneous and evoked activity of substantia nigra pars reticulata neurons during high-frequency stimulation of the subthalamic nucleus. *J Neurosci* 23:9929–9936.

68. Hamani C, Saint-Cyr JA, Fraser J, Kaplitt M, Lozano AM (2004) The subthalamic nucleus in the context of movement disorders. *Brain* 127:4–20.

69. Cury RG, et al. (2017) Thalamic deep brain stimulation for tremor in Parkinson disease, essential tremor, and dystonia. *Neurology* 89:1416–1423.

70. Ferraye MU, et al. (2010) Effects of pedunculopontine nucleus area stimulation on gait disorders in Parkinson's disease. *Brain* 133:205–214.

71. Lozano AM (2000) Vim thalamic stimulation for tremor. *Arch Med Res* 31:266–269.

72. Schuurman PR, et al. (2000) A comparison of continuous thalamic stimulation and thalamotomy for suppression of severe tremor. *N Engl J Med* 342:461–468.

73. Abosch A, et al. (2013) An international survey of deep brain stimulation procedural steps. *Stereotact Funct Neurosurg* 91:1–11.

74. Gross RE, Krack P, Rodriguez-Oroz MC, Rezai AR, Benabid AL (2006) Electrophysiological mapping for the implantation of deep brain stimulators for Parkinson's disease and tremor. *Mov Disord* 21(Suppl 14):S259–S283.

75. Priori A, et al. (2004) Rhythm-specific pharmacological modulation of subthalamic activity in Parkinson's disease. *Exp Neurol* 189:369–379.

76. Thompson JA, Lanctin D, Ince NF, Abosch A (2014) Clinical implications of local field potentials for understanding and treating movement disorders. *Stereotact Funct Neurosurg* 92:251–263.

77. Telkes I, Jimenez-Shahed J, Viswanathan A, Abosch A, Ince NF (2016) Prediction of STN-DBS electrode implantation track in Parkinson's disease by using local field potentials. *Front Neurosci* 10:198.

NEUROSCIENCE

Telkes et al.

www.manaraa.com

78. Contarino MF, et al. (2014) Directional steering: A novel approach to deep brain stimulation. *Neurology* 83:1163–1169.

79. Pollo C, et al. (2014) Directional deep brain stimulation: An intraoperative double-blind pilot study. *Brain* 137:2015–2026.

80. Bour LJ, et al. (2015) Directional recording of subthalamic spectral power densities in Parkinson's disease and the effect of steering deep brain stimulation. *Brain Stimul* 8:730–741.

81. Rouse AG, et al. (2011) A chronic generalized bi-directional brain-machine interface. *J Neural Eng* 8:036018.

82. Connolly AT, et al. (2015) Local field potential recordings in a non-human primate model of Parkinsons disease using the Activa PC + S neurostimulator. *J Neural Eng* 12:066012.

83. Jiang T, et al. (2017) A portable platform to collect and review behavioral data simultaneously with neurophysiological signals. *2017 39th Annual International Conference of the IEEE Engineering in Medicine and Biology Society (EMBC)* (Institute of Electrical and Electronics Engineers, Piscataway, NJ), pp 1784–1787.

84. Lachaux JP, Rodriguez E, Martinerie J, Varela FJ (1999) Measuring phase synchrony in brain signals. *Hum Brain Mapp* 8:194–208.

www.manaraa.com